Efficient photon extraction from a quantum dot in a broad-band planar cavity antenna

Efficient photon extraction from a quantum dot in a broad-band planar cavity antenna

Yong Ma, Peter E. Kremer, and Brian D. Gerardot

Citation: Journal of Applied Physics **115**, 023106 (2014); doi: 10.1063/1.4861723
View online: http://dx.doi.org/10.1063/1.4861723
View Table of Contents: http://scitation.aip.org/content/aip/journal/jap/115/2?ver=pdfcov
Published by the AIP Publishing

Efficient photon extraction from a quantum dot in a broad-band planar cavity antenna

Yong Ma,[a] Peter E. Kremer, and Brian D. Gerardot[b]
Institute of Photonics and Quantum Sciences, SUPA, Heriot-Watt University, Edinburgh EH14 4AS, United Kingdom

(Received 14 October 2013; accepted 24 December 2013; published online 10 January 2014)

We analyse the extraction of photons emitted from single InAs quantum dots embedded in planar microcavities. The structures are designed to achieve broad-band operation and high-collection efficiency from a device requiring straightforward fabrication, even with electrical contacts. The designs consist of a quantum dot in a GaAs membrane with asymmetric top and bottom mirrors and a top-side solid immersion lens (SIL). Four separate cases are considered in our design: a GaAs membrane only (case 1), GaAs membrane with a glass SIL on top (case 2), a GaAs membrane with a glass SIL on top and a back mirror consisting of Au (case 3), a GaAs membrane with a glass SIL on top of a distribute Bragg reflector mirror and Au back mirror (case 4). Both finite difference time domain and analytical simulations are used to calculate the electric field, power density, and far-field radiation pattern. For optimized structures (case 4), we obtain significant extraction efficiencies (>50%) with modest Purcell enhancements (~20%) and a large spectral full-width-half-maximum (>100 nm). The high-extraction efficiency, broad-band operation, and facile fabrication make the proposed structures promising for realistic quantum dot devices. © *2014 AIP Publishing LLC*. [http://dx.doi.org/10.1063/1.4861723]

I. INTRODUCTION

Semiconductor quantum dots (QDs) have attracted much recent attention for applications as quantum light sources.[1] In the simplest scenario, a QD can behave as a near-ideal mono-chromatic single photon emitter on-demand. Further functionality, including entangled photon pair generation[2] and spin initialization, manipulation, and read-out[3] as well as spin-photon entanglement,[4] can be obtained in multi-level QDs with multi-chromatic emission. Unfortunately, the collection efficiency, η, of light from a QD into an objective lens or single mode fiber is severely limited by two intrinsic obstacles: total internal reflection at the semiconductor–air interface and a large divergence angle of the escaping light in the far-field. For a QD in bulk GaAs, the escaping light has a critical angle of 16.7° and $\eta \sim 1\%$ even with a high numerical aperture (NA) optic. The most common approach to enhance η is to embed the QD in a high-Q cavity, such as a photonic crystal[5] or micropillar cavity[6,7] which enables a large Purcell enhancement factor (F_P) and tailorable far-field radiation profile but with the provision that the QD and cavity mode must spectrally and spatially overlap. However, self-assembled QDs naturally have a size distribution and therefore exhibit inhomogeneous broadening. Furthermore, unless heroic design and fabrication challenges are met,[2] a cavity's modes will not couple to the desired transitions in multi-level QDs. Hence, a less spectrally specific approach to enhance η is desirable for many applications. Recent broad-band successes include coupling a QD to a vertical nanowire wire[8,9] and in-plane waveguides.[10,11] A more moderately broad-band approach consisting of an optimized circular dielectric grating has also been recently demonstrated.[12] Alas, such structures require complicated fabrication, are spatially specific, and adding electrical control of the QD in such structures remains a considerable challenge.

In this paper, we analyze designs for realistic planar dielectric microcavities to modify the radiation pattern and power of single QDs to enable optimization of the extracted photon flux ($\eta \times F_p$) over a broad spectral range. The optimum design consists of a QD located at the anti-node of a second order GaAs membrane cavity with Au back reflector and an out-coupling distributed Bragg reflector (DBR) and glass solid-immersion lens (SIL) on top. η is optimized for an out-coupling DBR of GaAs/AlAs (two pairs with $\lambda/4$ thickness), where we find $\eta \sim 68\%$ (47%) into a free-space objective lens with NA = 1.0 (0.68) for emission centered at $\lambda = 950$ nm with a spectral full-width-half-maximum (FWHM) of ~120 nm. However, for this structure $F_P \sim 0.86$, thus inhibiting the overall photon flux extracted. We find that the choice of a TiO_2/SiO_2 DBR (three pairs with $\lambda/4$ thickness) yields the highest photon flux: $\eta \sim 50\%$ (41%) for NA = 1.0 (0.68) while $F_P \sim 1.2$ with a spectral FWHM of ~110 nm. Crucially, these designs maintain a suitable distance of the QD from any free surfaces and are straightforward to fabricate,[13] even with electrical contacts, as spatial control of the QD position with respect to the photonic structure is not required.

II. DESIGN CRITERIA

A crucial criteria for the design is to maintain the ~100% quantum efficiency typically observed in buried self-assembled QDs by protecting the dots from nearby free surfaces, ideally by more than 50 nm.[14] A secondary design criteria is to maintain the ability to easily incorporate

[a]y.ma@hw.ac.uk
[b]B.D.Gerardot@hw.ac.uk

electrical contacts, which allows the heterostructure functionality required for charge-tunable QD devices[15] or electrical injection of carriers.[16]

Our basic design, shown in Fig. 1, consists of a QD, represented by an electrical dipole with in-plane TE orientation, located a distance h from the top surface of a GaAs membrane of total thickness d sandwiched between two mirrors of thickness d_1 and d_2. The glass hemisphere SIL is used to increase the effective numerical aperture of the system and increase the critical angle of light which can be extracted from the device. This structure is inspired by resonant-cavity light-emitting diodes, which achieve high-efficiency light extraction from electrically contacted semiconductor light-emitting diodes with facile fabrication.[17,18] In our design, we place the dipole at the anti-node of a standing wave in the membrane with a thickness of the order of the emission wavelength. In this scenario, the membrane acts as a Fabry-Perot resonator in which the interference effects alter the internal angular power distribution.[19,20] The principle design challenge of the antenna to maximize the extraction efficiency is to have only one cavity mode, which is within the critical angle and can thus be coupled out of the device, and dominate the radiation pattern at the expense of guided modes which do not couple into the far-field.[19]

In addition to redistributing the dipole radiation pattern, the Fabry-Perot resonator can lead to an enhanced spontaneous emission rate due to the Purcell effect. However, due to the planar geometry, $F_P < 1.25$, for the designs considered here. Nevertheless, we show that in our optimized structures the light is extracted using a single resonance mode, demonstrating that the structure is clearly in the microcavity regime.[19] We also consider the use of out-coupling DBRs for mirror 1, as have been used in state-of-the-art experiments.[4,21,22] We note that the choice of SIL material presents a trade-off in the design: increasing n_{SIL} leads to a larger critical angle[23] but reduced reflectivity. In the extreme case of a GaAs SIL,[24] the cavity thickness is that of the membrane and SIL combined, eliminating the interference effects on the dipole radiation pattern unless a micro-SIL can successfully be fabricated.

Recently, Chen *et al.* have designed an optimal planar antenna for dipoles buried in GaAs which can remarkably extract a predicted 99% of the emitted light.[25] To realize this, several demanding conditions need to be satisfied: first, the GaAs membrane must be sandwiched between materials with suitably low refractive index to create a very strong cavity over large angles; second, the thickness of the GaAs membrane needs to be thin enough to suppress any guiding modes traveling within the membrane; and third, a SIL of ultra-high index material must be utilized to minimize index mismatch at the collection side. The first requirement can be met with an air gap above and below the GaAs membrane, possible with an AlAs sacrificial etch layer. Unfortunately, the second condition requires an ultra-thin membrane with the QD nearby free surfaces which would compromise the quantum efficiency due to non-radiative losses. The third condition could be met with a GaAs SIL which is possible but extremely challenging to fabricate. Finally, incorporating electrical contacts in such a device would be highly difficult. Therefore, we pursue here a design which enables 100% quantum efficiency, broad-band operation, and simple fabrication even with electrical contacts. The compromise is a reduced η. Nevertheless, compared to bulk structures, our antenna design offers a huge increase in η which is comparable to state-of-the-art micropillar[6,7] or nanowire[8,9] structures.

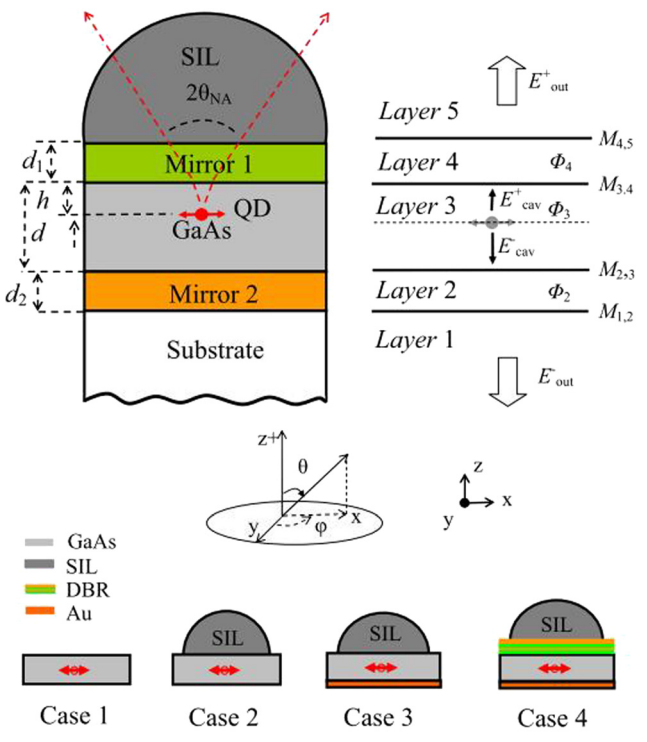

FIG. 1. Sketch of the considered structure: a quantum dot is embedded in a GaAs membrane sandwiched between two mirrors, and a SIL is attached on the top cavity mirror (mirror 1). θ_{NA} represents the angle corresponding to the numerical aperture of the collection optics. The analytical model parameters d, d_1, d_2, h, E^+_{out}, E^-_{out}, E^+_{cav}, E^-_{cav}, Φ_i, and $M_{i,j}$ are described in the text. Four separate cases are considered in our design: GaAs membrane only (case 1), a GaAs membrane with a glass SIL on top (case 2), a GaAs membrane with a glass SIL on top and a back mirror consisting of Au (case 3), a GaAs membrane with a glass SIL on top of a DBR and Au back mirror (case 4).

III. SIMULATION METHODS

We use both analytical modeling and finite difference time domain (FDTD) simulations to calculate the electrical field, power density, and η for a range of membrane thicknesses and mirror configurations. To elucidate the function of each structural component, we consider four separate cases: GaAs membrane only (case 1), GaAs membrane with a glass SIL on top (case 2), a GaAs membrane with a glass SIL on top and a back mirror consisting of Au (case 3), a GaAs membrane with a glass SIL on top of a DBR mirror and Au back mirror (case 4). The refractive indices at $T = 4\,K$ and $\lambda = 950\,nm$ of the SIL glass (*S-LAH79*, *AWI industries*), GaAs, AlAs, TiO_2, SiO_2, and Au are 2.00, 3.48, 3.14, 2.1, 1.45, and $0.235 + 6.438i$, respectively. To calculate η, an objective lens with numerical aperture $NA = 0.68$ is used unless otherwise noted.

The analytical model is based on the transfer matrix method,[26] which uses a dipole emission source term to

calculate the electrical field and power density $P(\theta, \varphi)$ in the direction (θ, φ) within a solid angle $d\Omega = \sin\theta\, d\theta\, d\varphi$, where φ is the azimuth angle from the x-axis and θ is the zenith angle from the positive z-axis, as shown in Fig. 1. The electric field in the structure is described by two matrices: the transfer matrix M at the boundary of two adjacent layers and a propagation matrix Φ through each layer

$$M_{i,i+1}^{TE,TM} = \frac{1}{t_{i,i+1}^{TE,TM}} \begin{bmatrix} 1 & r_{i,i+1}^{TE,TM} \\ r_{i,i+1}^{TE,TM} & 1 \end{bmatrix}, \tag{1}$$

$$\Phi_i(z) = \begin{bmatrix} \exp(ik_i z) & 0 \\ 0 & \exp(-ik_i z) \end{bmatrix}, \tag{2}$$

where i and $i+1$ are layer indices, r and t are reflection and transmission coefficients at the interface between layer i and $i+1$, TE and TM represent the two orthogonal polarization components of the electrical field, and k_i is the wave vector at layer i. We define layers $i = [1, 2, 3, 4, 5]$ as [air, air, GaAs, air, air] for case 1, [air, air, GaAs, SIL, SIL] for case 2, [GaAs, Au, GaAs, SIL, SIL] for case 3, and [GaAs, Au, GaAs, DBR, SIL] for case 4. The electrical field outside the cavity can be obtained by solving

$$\begin{bmatrix} A_\uparrow \\ A_\downarrow \end{bmatrix} = \Phi_3(h) M_{3,4} \Phi_4(d_1) M_{4,5} \begin{bmatrix} E_{out}^+ \\ 0 \end{bmatrix} - \Phi_3(d-h) M_{3,2} \Phi_2(d_2) M_{2,3} \begin{bmatrix} 0 \\ E_{out}^- \end{bmatrix}, \tag{3}$$

where E^+_{out} and E^-_{out} are the forward and backward electrical fields along the z-axis outside the cavity. d_1 and d_2 are the thickness of mirror 1 (layer 4) and mirror 2 (layer 2), respectively. At the dipole source plane, the electric fields in each vertical direction are determined by $A_{\uparrow,\downarrow}$, the normalized dipole source terms described in Ref. 26 which depend on the dipole orientation and polarization mode (TE or TM). The electric field at any position z inside the cavity can be written as

$$\begin{bmatrix} E_{cav}^+(z) \\ E_{cav}^-(z) \end{bmatrix} = \Phi_3(-z) M_{3,4} \Phi_4(d_1) M_{4,5} \begin{bmatrix} E_{out}^+ \\ 0 \end{bmatrix}. \tag{4}$$

The power density outside the cavity is then calculated using

$$P_{out}^{TE,TM}(\theta) = |E_{out}|^2 \frac{n_{out} k_{out}^2}{n_{cav} k_{cav}^2} = |E_{out}|^2 \frac{n^3{}_{out} \cos^2\theta_{out}}{n^3{}_{cav} \cos^2\theta_{cav}}. \tag{5}$$

Finally, η, is calculated by integrating the normalized power density $P_{out}(\theta)$ over the corresponding solid angle

$$\eta = \frac{\int_0^{2\pi} d\phi \int_0^{\theta_{NA}} P_{out} \sin\theta d\theta}{\int_0^{2\pi} d\phi \int_0^{\pi} P_{dipole} \sin\theta d\theta}, \tag{6}$$

where the dominator in Eq. (6) is the total power emitted by the dipole in the cavity. Similarly, we can calculate the Purcell factor using

$$F_p = \frac{\int_0^{2\pi} d\varphi \int_0^{\pi} P_{dipole} \sin\theta d\theta}{\int_0^{2\pi} d\varphi \int_0^{\pi} P_{GaAs} \sin\theta d\theta}, \tag{7}$$

where the numerator and the denominator are the total power emitted by the dipole in the cavity and in the bulk GaAs, respectively.[26]

In addition, we use a FDTD tool to verify the calculated results from the analytical modeling method. In the FDTD model, a simulation region with size of 20 μm × 20 μm × 3 μm is used to cover the entire structure. A perfect absorbing boundary condition is used for the boundary of the simulation region. Cubic mesh cells with a side length of 25 nm are used to mesh-grid the simulation region, and finer mesh cells with side length of 5 nm are used around interfaces to ensure accurate simulation results.

IV. SIMULATION RESULTS

We re-express the geometric parameters d and h with a reduced cavity length $d' = 2dn_{\mathrm{GaAs}}/\lambda$ and reduced dipole position $h' = 2hn_{\mathrm{GaAs}}/\lambda$. As d' and h' are varied, a discrete set of maxima corresponding to cavity resonances for η appear (see Fig. 2(a) for case 3). Fig. 2(b) shows for each case the oscillations in η as a function of d' with a fixed dipole position, $h' = 1.0$. The maxima in η (5%, 23%, 35% for cases 1-3, respectively) occur for the smallest cavity orders ($d' = 2.00$, 2.16, 2.44, cases 1-3, respectively). The deviations from an integer d' are due to phase shifts at the reflecting surfaces. As d' increases, the maximum values for η

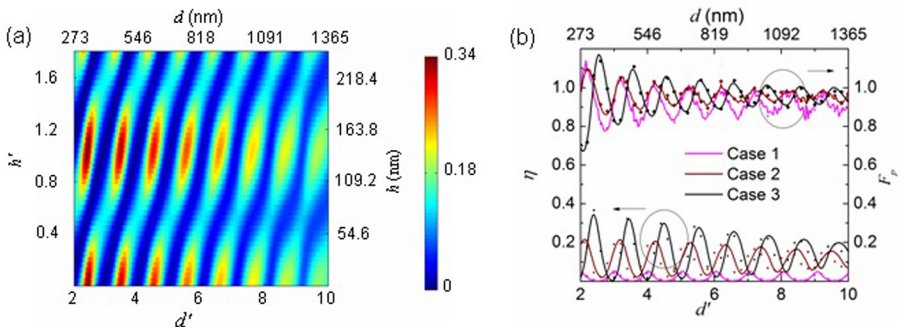

FIG. 2. (a) η as function of d (d') and h (h') for case 3; (b) η and F_p as function of d (d') for a given reduced dipole position at $h' = 1.0$ for cases 1, 2, and 3. Solid lines (points) are the analytical (FDTD) simulation results.

decrease as new guided modes which share the emitted power are introduced. For large d' (>100), η converges to 2%, 12%, and 15%, for cases 1-3, respectively. This convergence is due to the emitted power being evenly shared among a large number of modes which eventually form a continuum. We note that a so-called half-λ cavity ($d' \sim 1$) is not feasible for self-assembled QDs as the anti-node would be located at the cavity boundary. We also plot F_P as function of the cavity length for each case, as shown in Fig. 2(b). The Purcell factor varies for short cavity lengths and converges to ~1 for large d' due to decreased coupling between the dipole and the electric field.

To further clarify the physical mechanism for improved η in the optimized structures, we calculate the power density of the two independent polarized field components (*TE* and *TM*) of the dipole radiation as a function of the zenith angle θ in the far-field for cases 1-3 using a 2nd order cavity (Figs. 3(a) and 3(b)). For the *TE* modes in both cases 2 and 3 (Fig. 3(a)), the power density slowly increases from $\theta = 0$ to $\theta = \theta^{crit}{}_{SIL}$ due to the competing effects of phase resonance and reflectivity. For *TE* polarization, the phase resonance occurs at $\theta = 0$, but the reflectivity is minimized at this angle. As θ increases, the reflectivity increases while the phase resonance decreases. For the *TM* mode the same effects are present, but the power density reaches a minimum at the Brewster angle due to the minimized reflectivity (Fig. 3(b)). As a result, an emission pattern with "rabbit-ears" appears in the far-field outside the cavity for case 2. For case 3, the Au mirror provides near unity reflectivity over a broad range of incident angles, even at the Brewster angle, and the "rabbit-ears" are eliminated. This far-field profile allows only 1% collection efficiency into a single mode fibre (assuming

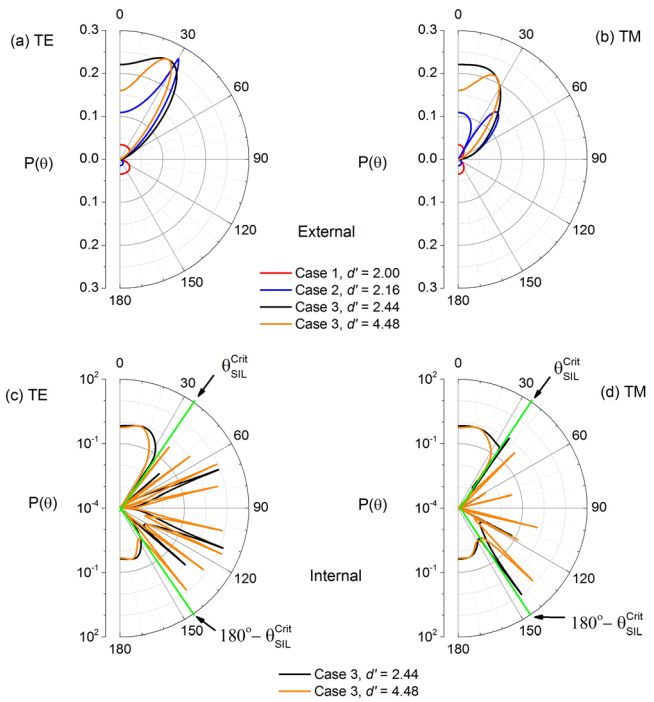

FIG. 3. Analytically simulated angular power distribution for *TE* (a), (c) and *TM* (c), (d) dipole radiation outside (a), (b) and inside (c), (d) the cavity for cases 1, 2, and 3. For case 3, we consider both a second ($d' = 2.44$) and a fourth ($d' = 4.48$) order cavity.

$NA_{sm} = 0.12$). We note that the power density inside the cavity for case 1 is higher than that for cases 2-3. However, the far-field power density is lower due to the transformation coefficient which is proportional to $(n^3{}_{out}/n^3{}_{cav})$ as shown in Eq. (5). Therefore, using a SIL with higher refractive index will further enhance the extractable emission.

We also highlight the effect of the cavity order on the dipole radiation pattern for both *TE* and *TM* polarizations inside the GaAs membrane for case 3 (Figs. 3(c) and 3(d), respectively). The phase shifts at the interfaces depend on the elevation angle (θ) and lead to a reduced spacing between adjacent resonance modes as a function of θ. Consequently, a total of $2 \times (\text{integer}(d') + 1)$ modes exist over $0 < \theta < 180°$ in the microcavity regime (e.g., there are 6 cavity modes present for $d' = 2.44$).[27] For $d' = 2.44$, the power density inside the cavity has a broad mode from $\theta = 0$ to $\theta \sim \theta^{crit}{}_{SIL}$, four sharper modes at $\theta^{crit}{}_{SIL} < \theta < (180° - \theta^{crit}{}_{SIL})$ which correspond to guided modes, and one broad mode at $(180° - \theta^{crit}{}_{SIL}) < \theta < 180°$ corresponding to the bulk absorption mode of the gold mirror. The out-coupled mode is a broad airy peak resulting from a planar cavity with modest Q. The power flow in the guided modes is assumed to be dissipated via surface plasmonic absorption in the metal layer and scattering at the edge of the membrane structure. As the cavity order is increased (e.g., $d' = 4.48$ in Figs. 3(c) and 3(d)), additional guided modes appear which decrease the total power emitted into the fundamental extracted mode. For case 3, the glass SIL increases the critical angle by nearly 100% over case 2, and the first mode is extracted from the cavity while the remaining modes are guided horizontally and not extracted.

Finally, we consider case 4 in which either AlAs/GaAs or TiO_2/SiO_2 DBRs are used for mirror 1.[4,21,22] While DBRs can provide high reflectivity, it is typically limited to relatively small incident angles ($\theta < 20°$ for 30 pairs of AlAs/GaAs DBR) and light at larger angles leaks through the mirror. Additionally, the DBR increases the effective cavity length, which introduces more cavity modes to share the emitted power with the extractable modes.[19] Conversely, Au has high reflectivity (>95%) independent of the incident angle. We therefore maintain Au for mirror 2 in case 4. However, a DBR improves the reflectivity of mirror 1 compared to the SIL–GaAs interface of case 3. As shown in Figs. 4(a) and 4(b), $\eta \sim 47\%$ (~41%) can be obtained by using two pairs of GaAs/AlAs DBRs (three pairs of TiO_2/SiO_2) as mirror 1, which is 12% (6%) more compared with that obtained from case 3. In addition, the cavity length d' and dipole position h' have slightly moved from $d' = 2.44$ and $h' = 1.00$ in case 3 to $d' = 2.52$ and $h' = 1.12$ ($d' = 2.44$ and $h' = 1.08$) for GaAs/AlAs (TiO_2/SiO_2) DBRs, as shown in Figs. 4(a) and 4(b). Fig. 4(c) shows η as function of N (number of DBR pairs) for optimized d' and h'. Fig. 4(d) shows the normalized power flux ($\eta \times F_P$) as a function of the N: the optimized $\eta \times F_P$ increases from 41% for GaAs/AlAs DBRs to 53% for TiO_2/SiO_2 DBRs because of the enhancement of F_P. Fig. 5 shows the analytically simulated angular power distributions for case 4. There is a strong resonance ("pencil-like" far-field beam profile) coupled out from the cavity at an oblique angle (~28°) for TiO_2/SiO_2 DBRs

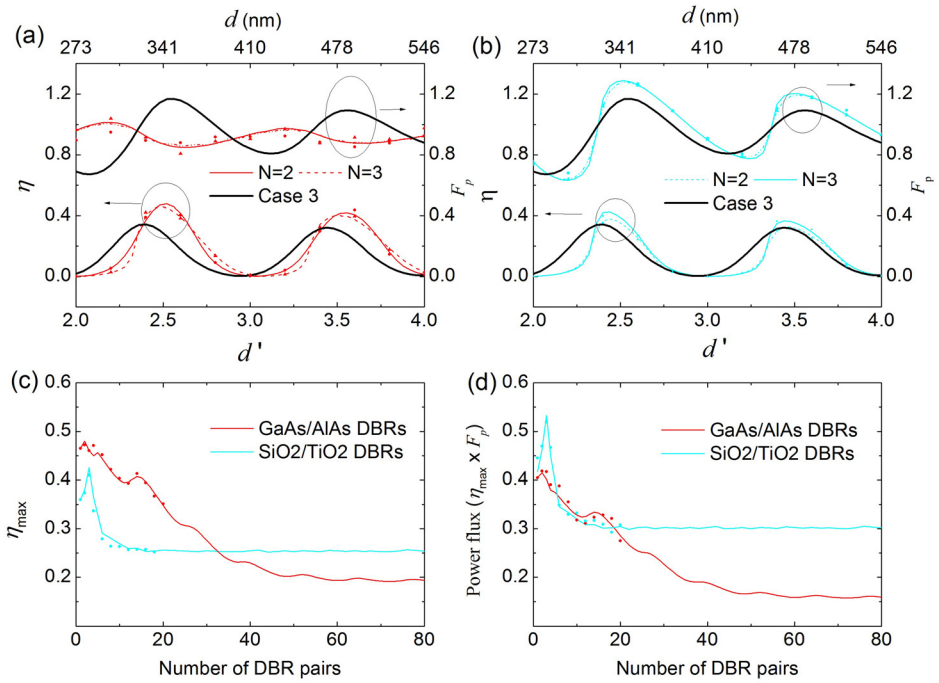

FIG. 4. (a) η and F_P as function of reduced cavity length d' for both two and three pairs of (a) AlAs/GaAs and (b) TiO_2/SiO_2 DBRs as mirror 1. (c) Comparison of (c) optimized collection efficiency η_{max} and (d) power flux ($\eta_{max} \times F_P$) between GaAs/AlAs and TiO_2/SiO_2 DBRs as function of the number of DBR pairs. The dipole source (QD) is placed at the first anti-node of the second order cavity for each structure. Solid lines (points) are the analytical (FDTD) simulation results.

(three pairs) and the total output emission within NA = 0.68 is much larger than GaAs/AlAs DBR (two pairs) due to the increased F_P. We note that the non-Gaussian far-field profile would be incompatible for collection with a single mode fibre. Figs. 5(c) and 5(d) show the internal power flow for each case, where we observe an increased number of radiating modes as well as enhanced power density for these modes for TiO_2/SiO_2 DBRs.

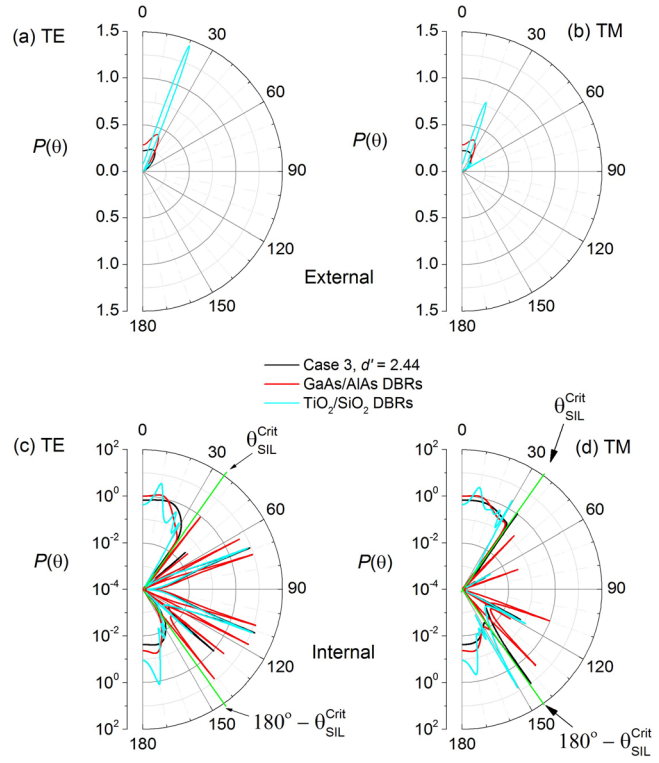

FIG. 5. Comparison of analytically simulated angular power distributions for *TE* (a), (c) and *TM* (c), (d) dipole radiation outside (a), (b) and inside (c), (d) the cavity for cases 3 and 4.

Finally, we show the relevant figures of merit as a function of NA and λ for each case in Fig. 6. Fig. 6(a) shows η as function of NA for each structure using an optimized second order cavity with $h' = 1.0$. A maximum η (NA = 1.0) as high as 68% is found for two pairs of GaAs/AlAs DBRs. Fig. 6(b) shows ($\eta \times F_P$) as a function of NA, with a maximum obtained TiO_2/SiO_2 DBRs (three pairs) with a high NA. Figs. 6(c) and 6(d) show the normalized collection efficiency and power flux as a function of optical wavelength for each case. Spectral bandwidths (FWHM) for cases 1-3 are ~150 nm for a design wavelength of $\lambda = 950$ nm. The spectral bandwidths for case 4 are slightly reduced to ~120 nm (~110 nm) for GaAs/AlAs (TiO_2/SiO_2) DBRs.

V. CONCLUSIONS

In this paper, the performance of planar microcavity antennas has been investigated by both FDTD and analytical modeling. To clarify the impact of each structural component on the extraction efficiency and Purcell factor, several separate cases were considered. The optimized design (case 4: a thin GaAs membrane with a top-side TiO_2/SiO_2 DBR and glass SIL and back-side Au mirror) yields $\eta \sim 41\%$ (for NA = 0.68), $F_P \sim 1.25$, and a spectral band-width of ~110 nm. Due to its high reflectivity independent of incidence angle, the gold mirror yields superior performance to a DBR for the back-side reflector (mirror 2). For the out-coupling mirror (mirror 1), the TiO_2/SiO_2 DBR has the highest reflectivity and best performance. Crucial for maximizing performance is maintaining a second order cavity with the QD located at the first antinode ($d \sim 333$ nm and $h = 147$ nm). Such a thin membrane can be fabricated using selective etching of an AlAs layer. This design also enables straightforward incorporation of electrical contacts: the Au mirror can be used as a Schottky contact while an ohmic contact can be remotely diffused to a highly doped layer

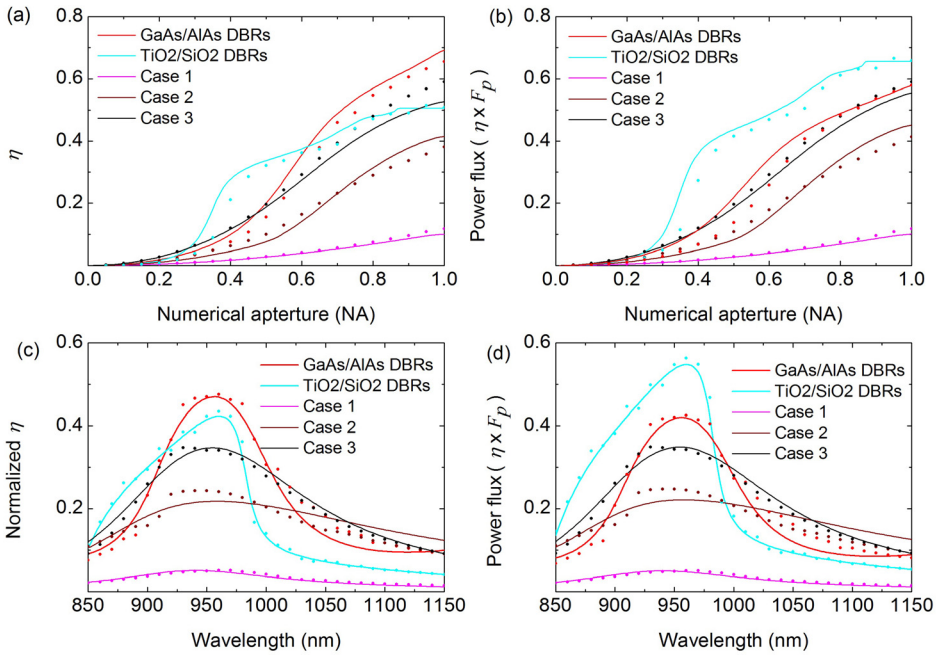

FIG. 6. For an optimized second order cavity with the dipole at the first antinode, we plot η and $\eta \times F_P$ as function of NA of the objective lens for $\lambda = 950$ nm [(a) and (b), respectively] or as a function of λ for NA = 0.68 [(c) and (d), respectively]. Solid lines (points) are the analytical (FDTD) simulation results.

grown above the dot layer (between the QDs and mirror 1), as shown in Fig. 7.

Comparing the planar dielectric cavities considered here to state-of-the-art structures with QDs embedded in tapered nanowires or high-Q cavities (e.g., photonic crystals or micropillars), we make the following observations. Significant advantages of the planar structure include: easy fabrication; no need for spatial (in-plane) positioning of the QDs with respect to a cavity or waveguide mode; easy incorporation of electrical contacts; broad-band operation enabling efficient coupling to multi-chromatic transitions or different QDs; and the elimination of nearby free surfaces which can cause spin or photon dephasing. Drawbacks of the planar structure are somewhat reduced η and significantly reduced F_P compared to QDs in nanowire waveguides or cavities. Further improvements in η can be realized for planar dielectric antennas with increased index of refraction of the solid immersion lens. In summary, optimized planar dielectric antenna designs have uncomplicated fabrication, even when incorporating electrical contacts, and are highly promising for efficient coupling between the far-field and multi-level transitions in quantum dots.

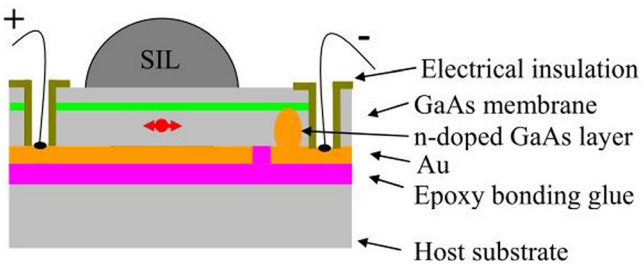

FIG. 7. Sketch of the fabricated membrane sample structure with both ohmic and Schottky contacts. The fabrication steps are (a) deposit 100 nm AuGe and 20 nm and anneal the sample at 400 °C to create an ohmic contact with the n-doped layer; (b) deposit 150 nm Au layer as Schottky contact and back reflecting mirror, leaving a 500 μm insulation gap between the ohmic contact and Schottky contact; (c) flip the sample and transfer it to a host substrate using an epoxy glue and compression; (d) selectively etch the bonded sample to remove GaAs substrate and AlGaAs sacrificial layer of the QD sample in sequence; (e) selectively etch the access areas for both contacts wiring; (f) wire both contacts using silver paint.

ACKNOWLEDGMENTS

We acknowledge funding from EPSRC (UK) and the Royal Society.

[1]A. J. Shields, Nat. Photonics **1**, 215 (2007).
[2]A. Dousse, J. Suffczyński, A. Beveratos, O. Krebs, A. Lemaître, I. Sagnes, J. Bloch, P. Voisin, and P. Senellart, Nature **466**, 217 (2010).
[3]A. Greilich, S. G. Carter, D. Kim, A. S. Bracker, and D. Gammon, Nat. Photonics **5**, 702 (2011).
[4]W. B. Gao, P. Fallahi, E. Togan, J. Miguel-Sanchez, and A. Imamoglu, Nature **491**, 426 (2012).
[5]M. Toishi, D. Englund, A. Faraon, and J. Vučković, Opt. Express **17**, 14618 (2009).
[6]S. Strauf, N. G. Stoltz, M. T. Rakher, L. A. Coldren, P. M. Petroff, and D. Bouwmeester, Nat. Photonics **1**, 704 (2007).
[7]O. Gazzano, S. M. de Vasconcellos, C. Arnold, A. Nowak, E. Galopin, I. Sagnes, L. Lanco, A. Lemaitre, and P. Senellart, Nat. Commun. **4**, 1425 (2013).
[8]J. Claudon, J. Bleuse, N. S. Malik, M. Bazin, P. Jaffrennou, N. Gregersen, C. Sauvan, P. Lalanne, and J. M. Gérard, Nat. Photonics **4**, 174 (2010).
[9]M. E. Reimer, G. Bulgarini, N. Akopian, M. Hocevar, M. B. Bavinck, M. A. Verheijen, E. P. A. M. Bakkers, L. P. Kouwenhoven, and V. Zwiller, Nat. Commun. **3**, 737 (2012).
[10]T. Lund-Hansen, S. Stobbe, B. Julsgaard, H. Thyrrestrup, T. Sünner, M. Kamp, A. Forchel, and P. Lodahl, Phys. Rev. Lett. **101**, 113903 (2008).
[11]M. Davanco, M. T. Rakher, W. Wegscheider, D. Schuh, A. Badolato, and K. Srinivasan, Appl. Phys. Lett. **99**, 121101 (2011).
[12]M. Davanço, M. T. Rakher, D. Schuh, A. Badolato, and K. Srinivasan, Appl. Phys. Lett. **99**, 041102 (2011).
[13]J. G. E. Harris, D. D. Awschalom, K. D. Maranowski, and A. C. Gossard, Rev. Sci. Instrum. **67**, 3591 (1996).
[14]C. F. Wang, A. Badolato, I. Wilson-Rae, P. M. Petroff, E. Hu, J. Urayama, and A. Imamoğlu, Appl. Phys. Lett. **85**, 3423 (2004).
[15]R. J. Warburton, C. Schäflein, D. Haft, F. Bickel, A. Lorke, K. Karrai, J. M. Garcia, W. Schoenfeld, and P. M. Petroff, Nature **405**, 926–929 (2000).
[16]Z. Yuan, B. E. Kardynal, R. M. Stevenson, A. J. Shields, C. J. Lobo, K. Cooper, N. S. Beattie, D. A. Ritchie, and M. Pepper, Science **295**, 102 (2002).

[17]H. De Neve, J. Blondelle, P. Van Daele, P. Demeester, R. Baets, and G. Borghs, Appl. Phys. Lett. **70**, 799 (1997).
[18]J. J. Wierer, D. A. Kellogg, and N. Holonyak, Appl. Phys. Lett. **74**, 926 (1999).
[19]H. Benisty, H. De Neve, and C. Weisbuch, IEEE J. Quantum Electron. **34**, 1612 (1998).
[20]A. Kastler, Appl. Opt. **1**, 17 (1962).
[21]A. J. Bennett, P. Atkinson, P. See, M. B. Ward, R. M. Stevenson, Z. L. Yuan, D. C. Unitt, D. J. P. Ellis, K. Cooper, D. A. Ritchie, and A. J. Shields, Phys. Status Solidi B **243**, 3730 (2006).
[22]R. Trotta, P. Atkinson, J. D. Plumhof, E. Zallo, R. O. Rezaev, S. Kumar, S. Baunack, J. R. Schroeter, A. Rastelli, and O. G. Schmidt, Adv. Mater. **24**, 2668 (2012).
[23]W. L. Barnes, G. Björk, J. M. Gérard, P. Jonsson, J. A. E. Wasey, P. T. Worthing, and V. Zwiller, Eur. Phys. J. D **18**, 197 (2002).
[24]A. N. Vamivakas, M. Atature, J. Dreiser, S. T. Yilmaz, A. Badolato, A. K. Swan, B. B. Goldberg, A. Imamoglu, and M. S. Ünlü, Nano Lett. **7**, 2892 (2007).
[25]X. W. Chen, S. Götzinger, and V. Sandoghdar, "99% efficiency in collecting photons from a single emitter," Opt. Lett. **36**, 3545–3547 (2011).
[26]H. Benisty, R. Stanley, and M. Mayer, J. Opt. Soc. Am. A **15**, 1192 (1998).
[27]D. Delbeke, R. Bockstaele, P. Bienstman, R. Baets, and H. Benisty, IEEE J. Quantum Electron. **8**, 189 (2002).